
Selection, Not Fusion: Radar-Modulated State Space Models for Radar-Camera Depth Estimation

Zhangcheng Hou

School of Science and Technology
Keio University
Yokohama 223-8522, Japan
zhangcheng@ohtsuki.ics.keio.ac.jp

Tomoaki Ohtsuki

School of Science and Technology
Keio University
Yokohama 223-8522, Japan
ohtsuki@ics.keio.ac.jp

Abstract

Radar-camera depth estimation must turn an ultra-sparse, all-weather, metric radar signal into a dense per-pixel depth map. Existing methods — concatenation, confidence-aware gating, sparse supervision, graph-based extraction — combine radar and image features outside the backbone’s sequence operator, and even cross-modal Mamba variants leave the selection mechanism itself unimodal. We argue that the selection mechanism is the right place for radar to enter. We introduce *Radar-Modulated Selection* (RMS), a minimal and principled way to inject radar into Mamba’s selective scan: radar modulates the scan from within, adding zero-initialised perturbations to the step size Δ and readout C while leaving the input projection B and state dynamics A image-only. The construction is exactly equivalent to a pretrained image-only Mamba at initialisation, ensuring radar only influences the model where it improves accuracy. Two further properties follow that out-of-scan fusion cannot offer: linear-cost cross-modal coupling at every recurrence step, and a natural fallback to the image-only backbone when radar is absent. We deploy RMS in a *Multi-View Scan Pyramid* (MVSP) that matches the fusion operator to radar’s spatial reach at each scale. SemoDepth achieves state-of-the-art performance on nuScenes, reducing MAE by 34.0%, 29.9%, and 29.9% over the previous best at 0–50, 0–70, and 0–80 m, while attaining the lowest single-frame latency (26.8 ms). A further ablation shows that out-of-scan feature blending adds no accuracy on top of RMS, providing empirical validation that in-scan selection can replace out-of-scan fusion.

1 Introduction

Dense per-pixel metric depth is foundational for autonomous driving Geiger et al. [2013], Caesar et al. [2020] and mobile robotics, supporting obstacle avoidance and localisation Adolfsson et al. [2022] as well as 3D object detection and bird’s-eye-view perception Lin et al. [2024], Chu et al. [2025]. Monocular cameras are cheap but inherently up-to-scale Yang et al. [2024] and degrade under rain, fog, and low light, while light detection and ranging (LiDAR) resolves scale at a power and cost budget that limits it to premium stacks. Millimetre-wave (77–81 GHz) frequency-modulated continuous-wave (FMCW) automotive radar bridges the gap: inexpensive, all-weather, directly metric, and ubiquitous in modern vehicles Bilik et al. [2019], Han et al. [2023], Caesar et al. [2020]. The signal itself, however, is severely limited: a nuScenes radar sweep contains only 40–100 returns in the front-camera field of view (FoV) — three orders of magnitude sparser than LiDAR — with angular and height ambiguities that emerging 4D radar datasets Palfy et al. [2022], Li et al. [2024a] only partially resolve.

Radar-camera depth completion Uhrig et al. [2017] has accumulated nearly a decade of designs: concatenation Lin et al. [2020], Long et al. [2021], Gasperini et al. [2021], Lo and Vandewalle [2021],

Singh et al. [2023], confidence-aware gating Sun et al. [2024], sparse supervision Li et al. [2024b], graph-based structure extraction Wang et al. [2025], and two-stage metric-scale refinement Li et al. [2024a]; in every case, radar and image features are combined at the feature level, outside the backbone’s sequence operator. In parallel, selective state-space models — Mamba Gu and Dao [2023], Dao and Gu [2024], Vim Zhu et al. [2024], VMamba Liu et al. [2024], MambaDepth Grigore and Popa [2024] — have replaced Transformers in vision via a token-level selection mechanism: an input-dependent step size Δ and readout \mathbf{C} that control what each token retains and emits. Existing cross-modal Mamba variants Xie et al. [2024], Li et al. [2024c] stack modality-specific streams before a shared scan, leaving the selection itself unimodal.

Selection, not fusion. We propose Radar-Modulated Selection (RMS), which injects radar inside Mamba’s Gu and Dao [2023] selective scan, and a Multi-View Scan Pyramid (MVSP) that matches the fusion operator to radar’s reach at each decoder resolution. SemoDepth, evaluated on nuScenes Caesar et al. [2020] and ZJU-4DRadarCam Li et al. [2024a], sets a new state-of-the-art on nuScenes mean absolute error (MAE) and root-mean-square error (RMSE) at every evaluation range (50 m, 70 m, 80 m). We further demonstrate that in-scan selection can replace out-of-scan fusion: out-of-scan feature blending adds no accuracy on top of RMS.

Our contributions are threefold:

- **Radar-Modulated Selection (RMS).** A principled mechanism that injects radar inside Mamba’s selective scan: radar contributes additive, zero-initialised modulations to the selection parameters Δ (per-token memory horizon) and \mathbf{C} (state readout), while the input projection \mathbf{B} and state dynamics \mathbf{A} stay image-only. Unlike feature-level fusion, which operates on static representations, in-scan selection directly modulates the recurrence dynamics that govern long-range information propagation. Radar therefore influences not only local feature composition but also the temporal evolution of memory within the sequence model, fundamentally changing how information is stored and propagated rather than merely how it is combined. Three advantages follow that prior out-of-scan fusion cannot offer: (i) *linear-cost cross-modal coupling* — radar shapes the recurrence at every token at $O(L)$ cost, never the $O(L^2)$ cost of cross-attention; (ii) *loss-preserving initialisation* — zero-init makes the block bit-equivalent to a vanilla Mamba scan at step zero, so the pretrained image-only solution is preserved exactly and radar gradient flows only where it earns accuracy; (iii) *image-only fallback* — with \mathbf{A} and \mathbf{B} unimodal, the model reduces to image-only behaviour under radar sparsity, without architectural reconfiguration.
- **Multi-View Scan Pyramid (MVSP).** A three-tier decoder that matches the fusion operator to radar’s reach at each resolution: scene-wide four-direction RMS at the coarsest scales (a linear-cost approximation of a Transformer’s 2-D receptive field), radar-centred windowed RMS at the mid scale (scan capacity spent only where radar supports the image), and constant-cost feature-wise linear modulation (FiLM) at the finest scales. Radar therefore stays live at every decoder level, with scan compute concentrated where radar evidence has the longest reach. An ablation that replaces the two scan tiers with FiLM degrades MAE@80 by 18%, confirming the allocation is load-bearing for accuracy, not merely an efficiency optimisation.
- **State-of-the-art on nuScenes.** SemoDepth sets a new state-of-the-art across MAE and RMSE at every evaluation range; a further ablation shows that out-of-scan feature blending on top of RMS adds no accuracy, providing empirical validation that in-scan selection can replace out-of-scan fusion.

2 Related work

2.1 Radar-camera depth estimation

Radar-camera depth estimation methods broadly fall into two families. *Two-stage* approaches such as RadarCam-Depth Li et al. [2024a] adapt a pretrained monocular depth estimator by learning a radar-conditioned correction of its metric scale, leaving the image backbone radar-agnostic. *Single-stage* methods train end-to-end from radar and image to dense depth, differing in how radar is injected into the image pipeline, typically through feature-level fusion before or after the backbone operator. Early work concatenates rasterised radar depth maps with the image channels, leaving fusion to be

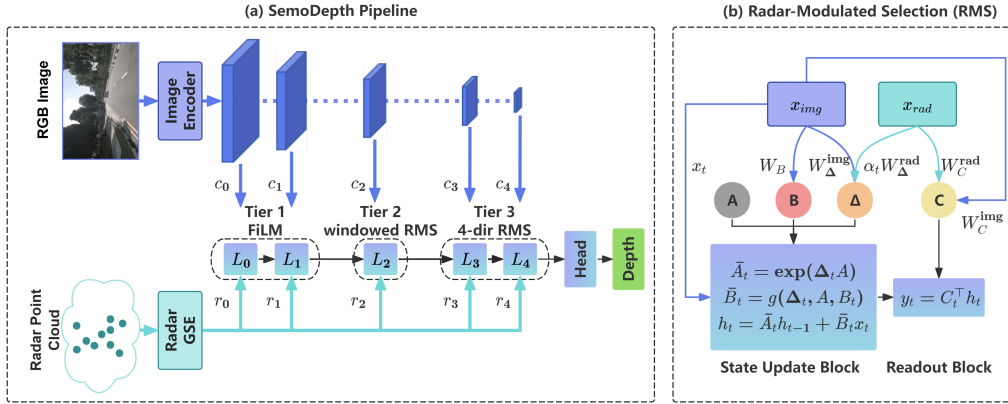


Figure 1: SemoDepth architecture. **(a) SemoDepth Pipeline.** A ResNet-34 image encoder and a PCA-GM Radar GSE produce the image pyramid c_0, \dots, c_4 and a single radar feature map whose level-wise 1×1 projections form the radar pyramid r_0, \dots, r_4 . The Multi-View Scan Pyramid (MVSP) allocates fusion by resolution: FiLM radar modulation at the two finest levels (Tier 1), windowed RMS around each projected radar return at the mid level (Tier 2), and full-image four-direction RMS at the two coarsest levels (Tier 3). **(b) Radar-Modulated Selection (RMS).** Radar enters via additive modulations to the step size Δ_t and readout C_t (dashed red), while the input projection B_t and state-evolution matrix A remain image-only (blue). The State Update Block performs zero-order hold (ZOH) discretization followed by the recurrence $\mathbf{h}_t = \bar{A}_t \mathbf{h}_{t-1} + \bar{B}_t x_t$; the Readout Block emits $y_t = C_t^T \mathbf{h}_t$. All radar projections are zero-initialised, so at step 0 the block reduces to vanilla Mamba.

learned implicitly by the network Lin et al. [2020], Long et al. [2021], Gasperini et al. [2021], Lo and Vandewalle [2021], Singh et al. [2023]. CaFNet Sun et al. [2024] introduces a confidence-aware gate that down-weights uncertain radar returns before mixing, addressing radar’s height and azimuth ambiguity. Li et al. Li et al. [2024b] sidestep densification entirely by supervising only at radar-visible pixels. TacoDepth Wang et al. [2025] extracts radar structure with a graph convolution network and attends image features through a radar-centred flash-attention pyramid, capturing long-range associations between radar points and supporting image regions.

2.2 Selective state-space models in vision

Selective state-space models (SSMs), introduced by Mamba Gu and Dao [2023], extend linear-time sequence modeling Gu et al. [2021] by making the recurrence parameters input-dependent per token: a *selective gate* controls each token’s memory horizon, and a *readout projection* determines what is extracted from the evolving hidden state. Vision backbones Vim Zhu et al. [2024], VMamba Liu et al. [2024], and MambaDepth Grigore and Popa [2024] adopt this design as a Transformer replacement. Prior cross-modal Mamba variants such as FusionMamba Xie et al. [2024] and MambaDFuse Li et al. [2024c] interact modalities by stacking or concatenating features before a shared Mamba block, so the selection parameters Δ and C are derived from a single fused representation rather than being explicitly conditioned on each modality, limiting cross-modal control within the selective state-space dynamics that govern long-range dependencies. SemoDepth instead injects radar directly into selection: Δ and C are computed from both modalities while the state update stays image-driven.

3 SemoDepth

3.1 Overview

SemoDepth is a single-stage radar-camera depth estimator (Fig. 1). A ResNet-34 image encoder, pretrained on ImageNet, produces five multi-scale feature maps c_0, \dots, c_4 at strides $\{1/2, 1/4, 1/8, 1/16, 1/32\}$ of the input resolution. In parallel, a *Radar GSE* (Graph Structure Extrac-

tor, following TacoDepth Wang et al. [2025]) processes the sparse radar point cloud — at most 512 returns per frame, each represented by image-normalised geometric coordinates $(y/H, x/W, d/d_{\max})$ with H, W the image height and width and d the return’s metric range. It employs a full-adjacency PCA-GM graph neural network Wang et al. [2019], originally developed for deep graph matching, and scatters its output into a per-pixel radar feature map. The image and radar streams remain unmixed prior to the selective scan: the radar map is downsampled to each decoder resolution and passed through a level-specific 1×1 projection, yielding the radar pyramid r_0, \dots, r_4 . The decoder comprises five levels L_0, \dots, L_4 , where level L_i fuses c_i with r_i via MVSP (§3.3). A direct-regression head maps the finest decoder feature to per-pixel metric depth, supervised by the composite objective of §3.4.

3.2 Radar-Modulated Selection (RMS)

We first describe RMS conceptually. The selective scan computes, per token, an input-dependent step size Δ_t (controlling how long each token’s content persists in the recurrence) and a readout vector C_t (controlling what is exposed from the latent state). In a vanilla cross-modal Mamba, both are derived from a single fused image-radar stream, so radar enters only as an additional input rather than as a control over selection. RMS modulates Δ_t and C_t directly: at every token, radar contributes a learned, zero-initialised correction to each, while the input projection B_t and the state-evolution matrix A remain image-only. The rest of this section makes the construction precise.

Let $\mathbf{x}_{\text{img}}, \mathbf{x}_{\text{rad}} \in \mathbb{R}^{B \times L \times D}$ denote the image and radar token streams from §3.1 (B = batch size, L = sequence length, D = channel dimension). A vanilla Mamba block Gu and Dao [2023] realizes a per-channel, per-token selective state-space recurrence on \mathbf{x}_{img} : for each of the D channels, a scalar input $x_t \in \mathbb{R}$ (one component of $\mathbf{x}_{\text{img},t}$) drives a hidden state $\mathbf{h}_t \in \mathbb{R}^N$ of state dimension N , producing a scalar output $y_t \in \mathbb{R}$ via

$$\mathbf{h}_t = \bar{\mathbf{A}}_t \mathbf{h}_{t-1} + \bar{\mathbf{B}}_t x_t, \quad y_t = \mathbf{C}_t^\top \mathbf{h}_t, \quad (1)$$

for $t = 1, \dots, L$. The discretized matrices $\bar{\mathbf{A}}_t = \exp(\Delta_t \mathbf{A})$ and $\bar{\mathbf{B}}_t = (\Delta_t \mathbf{A})^{-1} (\exp(\Delta_t \mathbf{A}) - \mathbf{I}) \Delta_t \mathbf{B}_t$ are obtained by zero-order hold (ZOH) integration from a trainable, token-independent matrix $\mathbf{A} \in \mathbb{R}^{D \times N}$ with negative-definite spectrum, where \mathbf{I} is the identity. The three remaining quantities $\Delta_t \in \mathbb{R}^D$, $\mathbf{B}_t \in \mathbb{R}^N$, $\mathbf{C}_t \in \mathbb{R}^N$ are produced per token by linear projections of the image stream,

$$\Delta_t = \tau_\Delta (\mathbf{W}_\Delta^{\text{img}} \mathbf{x}_{\text{img},t}), \quad \mathbf{B}_t = \mathbf{W}_B \mathbf{x}_{\text{img},t}, \quad \mathbf{C}_t = \mathbf{W}_C^{\text{img}} \mathbf{x}_{\text{img},t}, \quad (2)$$

where $\mathbf{W}_\Delta^{\text{img}}, \mathbf{W}_B, \mathbf{W}_C^{\text{img}}$ are trainable linear maps whose output shapes match $\Delta_t, \mathbf{B}_t, \mathbf{C}_t$ respectively, and $\tau_\Delta = \text{softplus}$ enforces $\Delta_t > \mathbf{0}$. From a control-theoretic perspective, the selective scan has three input-dependent parameters per token — Δ_t (step size), \mathbf{B}_t (input projection), and \mathbf{C}_t (readout). \mathbf{B}_t governs controllability (how inputs enter the system), \mathbf{C}_t determines observability (which aspects of the hidden state are exposed), and Δ_t sets the memory timescale of the recurrence. By modulating Δ_t and \mathbf{C}_t while keeping \mathbf{B}_t image-only, RMS preserves the semantic integrity of image features and lets radar selectively influence (i) temporal credit assignment via Δ_t and (ii) observation via \mathbf{C}_t — the two fundamental degrees of freedom over selection.

3.2.1 Horizon modulation

We modulate the memory horizon by perturbing the step size Δ_t , allowing radar to locally adjust how far information is propagated along the sequence. Concretely, the horizon pathway adds a radar-driven contribution to the pre-softplus step size, gated by a scalar $\alpha_t \in \mathbb{R}$:

$$\Delta_t = \tau_\Delta (\mathbf{W}_\Delta^{\text{img}} \mathbf{x}_{\text{img},t} + \alpha_t \odot \mathbf{W}_\Delta^{\text{rad}} \mathbf{x}_{\text{rad},t}), \quad \alpha_t = \sigma (\mathbf{W}_g \mathbf{x}_{\text{rad},t} + b_g), \quad (3)$$

where $\sigma(u) = (1 + e^{-u})^{-1}$ is the logistic sigmoid, \odot denotes the elementwise (Hadamard) product with α_t broadcast over the D channels of the radar projection, $\mathbf{W}_\Delta^{\text{rad}}$ is a linear map with the same output shape as $\mathbf{W}_\Delta^{\text{img}}$, and $\mathbf{W}_g \in \mathbb{R}^{1 \times D}$, $b_g \in \mathbb{R}$ form the scalar gate. We set $b_g = -2$ and zero-initialize $\mathbf{W}_\Delta^{\text{rad}}$ and \mathbf{W}_g . Since $\bar{\mathbf{A}}_t = \exp(\Delta_t \mathbf{A})$ interpolates between long-range state retention as $\Delta_t \rightarrow \mathbf{0}$ and short-range reset-and-focus behaviour as $\Delta_t \rightarrow \infty$ Gu and Dao [2023], the horizon pathway lets radar steer this trade-off locally; the initialization $\alpha_t|_{\text{init}} = \sigma(-2) \approx 0.12$ keeps the modulation latent at epoch zero so training opens it only if it helps.

3.2.2 Readout modulation

The readout pathway augments \mathbf{C}_t additively,

$$\mathbf{C}_t = \mathbf{W}_C^{\text{img}} \mathbf{x}_{\text{img},t} + \mathbf{W}_C^{\text{rad}} \mathbf{x}_{\text{rad},t}, \quad (4)$$

where $\mathbf{W}_C^{\text{rad}}$ is a linear map with the same \mathbb{R}^N output shape as $\mathbf{W}_C^{\text{img}}$, and is zero-initialized. In contrast to horizon modulation, which affects how information is stored, readout modulation reshapes what is extracted from the state: because the emission in Eq. (1) reads out the hidden state as $y_t = \mathbf{C}_t^\top \mathbf{h}_t$, the added radar term changes what each token reports without altering what the recurrence stored. No scalar gate is required, since the projection itself opens only under gradient.

3.2.3 Joint modulation

The full RMS block superposes both pathways, combining Eq. (3) and Eq. (4) in a single Mamba layer. At initialization the radar projections are zero maps, $\mathbf{W}_\Delta^{\text{rad}} = \mathbf{W}_C^{\text{rad}} = \mathbf{0}$, so

$$\Delta_t|_{\text{init}} = \tau_\Delta(\mathbf{W}_\Delta^{\text{img}} \mathbf{x}_{\text{img},t}), \quad \mathbf{C}_t|_{\text{init}} = \mathbf{W}_C^{\text{img}} \mathbf{x}_{\text{img},t}, \quad (5)$$

which reproduces the image-only selection of Eq. (2) exactly, so the recurrence collapses pointwise to baseline Mamba at epoch zero — a property we verify numerically.

3.3 Multi-View Scan Pyramid (MVSP)

Applying RMS uniformly at every decoder tier is computationally inefficient. Scan cost grows linearly with token count, exceeding 10^5 tokens per direction at the finest tiers, while radar’s effective spatial support shrinks with scale, so the heaviest compute would fall where radar contributes least. MVSP matches the fusion operator at each decoder level to the reach of radar evidence at that resolution. At the two coarsest tiers, full-image four-direction RMS aggregates scene-wide context, approximating a 2D receptive field at linear cost. At the mid tier, RMS is restricted to windows centred on each projected radar return, so scan capacity is spent only where radar actually supports the image. At the two finest tiers, RMS gives way to FiLM radar modulation at constant per-pixel cost, preserving an active radar signal into the full-resolution decoder without paying scan cost at the tiers where it grows fastest.

3.4 Training objective

The objective balances the robustness of noisy, dense supervision with the accuracy of clean, sparse measurements. Let \mathbf{D}_{pred} , \mathbf{D}_{main} , and $\mathbf{D}_{\text{sparse}}$ denote the prediction, main supervision target, and an optional clean sparse target. On nuScenes Caesar et al. [2020], $\mathbf{D}_{\text{main}} = \mathbf{D}_{\text{acc}}$ (160-sweep accumulated, dense but noisy) and $\mathbf{D}_{\text{sparse}} = \mathbf{D}_{\text{gt}}$ (single-sweep, clean); on ZJU-4DRadarCam Li et al. [2024a], \mathbf{D}_{main} is the dataset’s interpolated dense depth and no $\mathbf{D}_{\text{sparse}}$ is supplied. Depths are log-normalised to $\tilde{d} \in [-1, 1]$ over $[d_{\text{min}}, d_{\text{max}}]$ and each loss is masked to the valid pixels of its target. The composite objective

$$\mathcal{L} = \lambda_{\text{log}} \mathcal{L}_{\text{log}} + \lambda_{\text{lin}} \mathcal{L}_{\text{lin}} + \lambda_{\text{grad}} \mathcal{L}_{\text{grad}} + \lambda_{\text{sparse}} \mathcal{L}_{\text{sparse}} \quad (6)$$

combines a log-L1 \mathcal{L}_{log} against $\mathbf{D}_{\text{sparse}}$ (falling back to \mathbf{D}_{main} when the sparse target is unavailable), a Huber loss \mathcal{L}_{lin} ($\delta = 5$ m) against \mathbf{D}_{main} normalised by d_{max} , an L1 $\mathcal{L}_{\text{grad}}$ on the x, y gradients of $\tilde{\mathbf{D}}_{\text{pred}} - \tilde{\mathbf{D}}_{\text{main}}$, and a linear-metre L1 $\mathcal{L}_{\text{sparse}}$ against $\mathbf{D}_{\text{sparse}}$ normalised by d_{max} (echoing the sparse L1 term of TacoDepth Wang et al. [2025], active only when $\mathbf{D}_{\text{sparse}}$ is supplied). Confining log-space to the clean target and clipping linear residuals at 5 m keeps tail-pixel residuals from dominating gradients. We set $\lambda_{\text{log}} = \lambda_{\text{lin}} = \lambda_{\text{sparse}} = 1.0$ and $\lambda_{\text{grad}} = 0.5$ throughout.

4 Experiments

We conduct experiments on the nuScenes Caesar et al. [2020] and ZJU-4DRadarCam Li et al. [2024a] datasets, following prior radar-camera depth work Li et al. [2024a], Wang et al. [2025], Sun et al. [2024], Li et al. [2024b], Singh et al. [2023], Lin et al. [2020], Long et al. [2021], Gasperini et al. [2021], Lo and Vandewalle [2021].

4.1 Datasets and evaluation protocols

nuScenes. The nuScenes dataset Caesar et al. [2020] comprises 1,000 outdoor driving scenes and roughly 40,000 synchronised radar-camera keyframes collected in Boston and Singapore with a vehicle-mounted platform (camera, 3D radar, LiDAR, and inertial measurement unit). We adopt the standard 700/150/150 train / val / test scene split used by prior work Li et al. [2024a], Wang et al. [2025], Sun et al. [2024], Li et al. [2024b], Singh et al. [2023]. Each front-camera image is 900×1600 ; each radar frame contains 40–100 returns in the camera FoV.

ZJU-4DRadarCam. ZJU-4DRadarCam Li et al. [2024a] comprises 33,409 keyframes collected by a ground robot equipped with a higher-resolution camera, a 4D radar, and a denser LiDAR. We follow the official 29,312/4,097 train+val / test split. Following prior work Li et al. [2024a], Wang et al. [2025], we crop images from 720×1280 to 300×1280 to remove hood and sky regions.

Protocols and metrics. Following prior work Li et al. [2024a], Wang et al. [2025], Sun et al. [2024], Li et al. [2024b], we evaluate at three depth ranges — 0–50 m, 0–70 m, and 0–80 m — against single-sweep sparse LiDAR ground truth. We report MAE and RMSE as primary accuracy metrics, complemented by their inverse-depth analogues — inverse-depth MAE (iMAE) and inverse-depth RMSE (iRMSE), computed on $1/\hat{D}$ vs. $1/D_{\text{gt}}$ in km^{-1} — on the ZJU comparison and the ablation tables, where tail-pixel behaviour is most informative.

4.2 Implementation details

Data processing. On nuScenes, the dense main target D_{acc} is formed by accumulating D_{gt} over 160 nearby frames following Wang et al. [2025], Li et al. [2024b], with a light upper-image filtering pass to suppress accumulation artefacts in the supervision target (model inputs are unchanged). On ZJU-4DRadarCam, D_{acc} is the dataset’s interpolated dense depth from Li et al. [2024a]; no filtering is applied.

Hyperparameters. Referring to the architecture introduced in §3, the Radar GSE uses three PCA-GM layers with hidden dimension 64. The two coarsest MVSP tiers stack two RMS layers each; the mid tier uses window size $w = 8$ with Gaussian scatter weighting $\sigma = w/2.5$.

Training recipe. We train with Adam at an initial learning rate of 10^{-4} , following the additive step-decay schedule of TacoDepth Wang et al. [2025]: the rate is reduced by an absolute step of 10^{-5} every ten epochs and floored at $0.5 \times$ the initial rate. Training runs for 50 epochs with batch size 12 under bf16 autocast. The model’s depth range $[d_{\text{min}}, d_{\text{max}}]$ is $[0.5, 120]$ m on nuScenes and $[0.5, 80]$ m on ZJU-4DRadarCam; the nuScenes ceiling is set to 120 m so that the roughly 15% of radar returns in the 80–120 m band are not compressed against an artificial boundary during training, while evaluation uses a maximum range of 80 m on both datasets. Loss weights are as given in §3.4. For the main configuration in Table 1, we report the mean and standard deviation over three independently seeded training runs. All methods compared in §4.3 are evaluated under identical input resolution, evaluation ranges, and ground-truth protocol.

4.3 Comparisons with state-of-the-art methods

Table 1 compares SemoDepth against eight independent radar-camera depth baselines on the nuScenes dataset under the TacoDepth Wang et al. [2025] training and evaluation protocol — identical train/val/test split, 900×1600 input, single-sweep sparse LiDAR ground truth, and the same three evaluation ranges. We additionally include a Mamba-based fusion baseline by re-implementing FusionMamba Xie et al. [2024] for radar-camera depth completion (denoted with † in Table 1); FusionMamba was originally proposed for multimodal image fusion and has no published radar-camera depth result, so we adapt its dual-encoder visual state-space model (VSSM_Fusion) backbone with cross-modal selective-scan-2D (SS2D) fusion at every scale, train it under the same supervision, optimiser, and loss as SemoDepth, and tune its width to a matched ≈ 38 M-parameter budget. Baseline MAE and RMSE for the eight published methods are taken from each method’s original publication; the FusionMamba row reports the best-MAE@80 checkpoint of our re-implementation. Inference times for baselines whose code and weights are publicly available are re-measured on identical hardware (NVIDIA RTX PRO 6000 Blackwell, batch 1, FP32, 900×1600 input, mean over 100 iterations after 10 warmup) so that the efficiency comparison is conducted under matched conditions; baselines without a runnable release are reported as “—”.

Table 1: Quantitative comparisons with state-of-the-art radar-camera depth estimation methods on the nuScenes dataset Caesar et al. [2020]. MAE and RMSE are reported at three depth ranges; Time is single-frame inference latency. Baseline MAE and RMSE are taken from each method’s original publication; Time values are re-measured on identical hardware where a runnable release exists, otherwise reported as “–”. †FusionMamba was originally proposed for multimodal image fusion; we re-implement its VSSM_Fusion backbone (dual encoder pyramids, cross-modal SS2D fusion at every scale, decoder pyramid) for radar-camera depth completion under matched parameter budget, supervision, optimiser, and loss, as a modern Mamba-based fusion baseline. Best per column in **bold**.

Method	Time (ms)↓	0–50 m		0–70 m		0–80 m	
		MAE (mm) ↓	RMSE (mm) ↓	MAE (mm) ↓	RMSE (mm) ↓	MAE (mm) ↓	RMSE (mm) ↓
Lin et al. Lin et al. [2020] (IROS’20)	–	2034.9	4316.5	2294.7	5338.2	2371.0	5623.0
RC-PDA Long et al. [2021] (CVPR’21)	145.0	2225.0	4156.5	3326.1	6700.6	3713.6	7692.8
R4Dyn Gasperini et al. [2021] (3DV’21)	–	–	–	–	–	–	6434.0
DORN Lo and Vandewalle [2021] (ICIP’21)	60.9	1926.6	4124.8	2380.6	5252.7	2467.7	5554.3
Singh et al. Singh et al. [2023] (CVPR’23)	40.9	1727.7	3746.8	2073.2	4590.7	2179.3	4898.7
CaFNet Sun et al. [2024] (IROS’24)	44.2	1674.2	3674.5	2010.3	4493.1	2109.8	4765.6
Li et al. Li et al. [2024b] (ECCV’24)	46.4	1524.5	3567.3	1822.9	4303.6	1927.0	4609.6
FusionMamba† Xie et al. [2024] (VI’24)	–	1179.9	3337.2	1483.3	4282.5	1590.5	4640.0
TacoDepth Wang et al. [2025] (CVPR’25)	–	1423.6	3275.8	1712.6	3960.5	1833.4	4150.2
SemoDepth (Ours)	26.8	940.1\pm4.1	2785.7\pm2.5	1199.8\pm1.5	3622.4\pm16.5	1285.2\pm0.9	3935.4\pm21.5

SemoDepth achieves the lowest MAE and the lowest RMSE at every evaluation range. To put the magnitude in context, the seven prior baselines span a cumulative MAE@80 reduction of roughly 540 mm across nearly half a decade of progress (from 2371 mm in Lin et al. to 1833 mm in TacoDepth); SemoDepth improves on TacoDepth by an additional 548 mm in a single architectural step — comparable in magnitude to the cumulative span of prior progress under the same evaluation protocol. The architectural gain dominates the supervision-processing contribution: even trained on raw 160-sweep supervision without our upper-image filtering pass (§4.2), Joint-Modulation SemoDepth attains MAE@80 = 1311.9 mm — a 28.5% reduction over TacoDepth (1833.4 mm), within 2% of the cleaned-supervision headline. Per-variant raw-vs-cleaned numbers are in §A.5.

Two patterns in Table 1 tie the result to the design claims of §3. (i) MAE improvements are more than twice as large as RMSE improvements at every range (34.0% vs. 15.0% at 0–50 m, 29.9% vs. 8.5% at 0–70 m, and 29.9% vs. 5.2% at 0–80 m). The asymmetry reflects how each metric weights pixels: RMSE emphasises tail outliers, while MAE reflects the typical pixel. The accumulated gain therefore accrues to the typical pixel rather than the worst case — consistent with the behaviour expected from in-scan selection. By reshaping Δ and C at every token, RMS lets each radar return’s metric anchor propagate through the full sequence rather than only the local neighbourhood of its projected pixel, a token-level reshaping that is difficult to achieve with out-of-scan fusion alone. (ii) The gap to TacoDepth is the most informative cross-method comparison. TacoDepth’s radar-centred windowed flash-attention is architecturally closest to SemoDepth’s mid-tier windowed RMS, so the consistent \sim 30% MAE margin at every range is unlikely to be explained by windowed processing alone. The remaining gap is consistent with MVSP’s two distinguishing tiers — scene-wide four-direction RMS at the coarsest scales (no analogue in TacoDepth’s pyramid) and constant-cost FiLM that keeps radar live at the finest scales (where TacoDepth’s pyramid attenuates). A second informative comparison is to FusionMamba. Our re-implemented FusionMamba (Table 1, †), trained with matched supervision, optimiser, and loss, lands at MAE@80 = 1591 mm — between TacoDepth and SemoDepth. A Mamba backbone alone therefore closes part of the gap to SemoDepth, but a 19.2% MAE@80 margin remains. With the backbone family held fixed at Mamba and the training pipeline matched, this margin isolates the contribution of *in-scan* selection over pre-scan fusion: the same architectural distinction made in §2.2, now visible as a quantitative gap rather than a design argument. Fig. 2 provides representative Night/Day/Rain qualitative comparisons against the three baselines with publicly available code (CaFNet Sun et al. [2024], Li et al. Li et al. [2024b], Singh et al. Singh et al. [2023]).

ZJU-4DRadarCam. Table 2 reports results against the three baselines compared by TacoDepth Wang et al. [2025]. SemoDepth attains the best MAE at every evaluation range and the best RMSE@50; TacoDepth retains a slight edge on RMSE@70 (+1.4%) and RMSE@80 (+2.1%). The pattern mirrors the nuScenes result — 5–8% MAE drops over TacoDepth, with a small tail of outliers keeping RMSE within 2.1% of the closest baseline.

Table 2: Quantitative comparisons with state-of-the-art radar-camera depth estimation methods on the ZJU-4DRadarCam dataset Li et al. [2024a]. MAE and RMSE are reported at three depth ranges. Baseline numbers are as reported by TacoDepth Wang et al. [2025]. Best per column in **bold**.

Method	0–50 m		0–70 m		0–80 m	
	MAE (mm) ↓	RMSE (mm) ↓	MAE (mm) ↓	RMSE (mm) ↓	MAE (mm) ↓	RMSE (mm) ↓
DORN Lo and Vandewalle [2021]	2210.2	4129.7	2402.2	4625.2	2447.6	4760.0
Singh et al. Singh et al. [2023]	1785.4	3704.6	1932.7	4137.1	1979.5	4309.3
TacoDepth Wang et al. [2025]	1120.1	2686.7	1181.8	2906.3	1201.1	2990.7
SemoDepth (Ours)	1029.2	2631.6	1111.6	2946.9	1137.2	3053.0

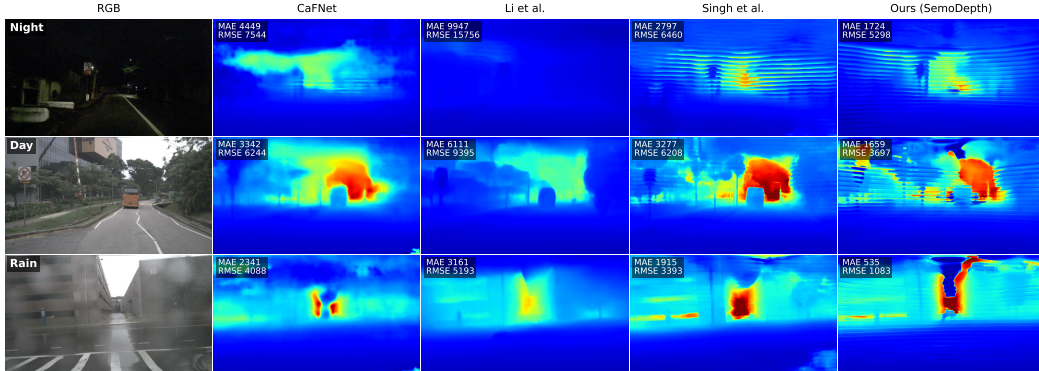


Figure 2: Qualitative comparison with state-of-the-art radar-camera depth estimation methods on the nuScenes dataset Caesar et al. [2020]. Rows: *Night* (frame 5319), *Day* (frame 161), *Rain* (frame 3088). Columns: RGB, CaFNet Sun et al. [2024] (IROS’24), Li et al. Li et al. [2024b] (ECCV’24), Singh et al. Singh et al. [2023] (CVPR’23), SemoDepth (Ours). Per-frame MAE / RMSE are reported in millimetres against single-sweep sparse LiDAR over 0–80 m; the jet colormap is clipped at 80 m. SemoDepth wins MAE and RMSE on every frame, with the largest margin on *Rain* (535 vs. 1915 mm MAE for the next-best baseline).

4.4 Inference efficiency

SemoDepth attains the lowest single-frame latency among methods with public releases (26.8 ms), 1.5–2.3× faster than Singh et al., CaFNet, Li et al., and DORN. It is heavier than TacoDepth in parameters but sits mid-pack on FLOPs; the latency advantage follows from MVSP’s tiered allocation (§3.3), which restricts scan compute to the coarser tiers.

4.5 Ablation studies

Table 4 ablates the two architectural pillars of SemoDepth. All variants share the same ResNet-34 encoder, Radar GSE, training recipe (§4.2), and depth range; only the decoder and the in-scan fusion pathway differ.

MVSP is critical for accuracy, not merely a computational convenience. The *Uniform FiLM* row replaces MVSP’s Tier 2 and Tier 3 Mamba-based scans with constant-cost FiLM modulation at every decoder level, keeping every other architectural component fixed. The remaining Joint-Modulation row improves MAE@80 from 1564 to 1286 (–18%). The pyramid therefore plays a central role in accuracy.

Both RMS pathways contribute. Within the MVSP framework, Horizon Modulation and Readout Modulation each recover a substantial portion of the Uniform-FiLM-to-Joint gap, confirming that the pathways are not redundant. The complementary behaviour suggests that horizon modulation (§3.2.1) controls information flow through the recurrence, while readout modulation (§3.2.2) controls information extraction at the emission step, and their combination is necessary for full cross-modal expressivity. Joint Modulation attains the lowest MAE@80 (1286 vs. 1352 Horizon-only, 1317

Table 3: Inference efficiency on the nuScenes dataset Caesar et al. [2020]. Time is re-measured under the Table 1 protocol; TacoDepth has no public release (Time reported as “-”). Params and FLOPs are from the TacoDepth paper for DORN, Singh et al., and TacoDepth, and re-measured (thop, $2\times$ MACs) for CaFNet and Li et al.; SemoDepth FLOPs are an fvcore lower bound. Best per column in **bold**.

Method	Params (M) ↓	FLOPs (G) ↓	Time (ms) ↓
DORN Lo and Vandewalle [2021] (ICIP’21)	183.4	923.5	60.9
Singh et al. Singh et al. [2023] (CVPR’23)	22.8	502.1	40.9
CaFNet Sun et al. [2024] (IROS’24)	62.2	1426.6	44.2
Li et al. Li et al. [2024b] (ECCV’24)	36.9	31.0	46.4
TacoDepth Wang et al. [2025] (CVPR’25)	13.5	139.3	-
SemoDepth (Ours)	38.1	271.8	26.8

Table 4: Ablation on the nuScenes dataset Caesar et al. [2020]. *Uniform FiLM* replaces the Tier 2 and Tier 3 Mamba-based scans with constant-cost FiLM modulation at every decoder level. *Horizon Modulation*, *Readout Modulation*, and *Joint Modulation* denote the three RMS variants of §3.2; *RMS + pre-scan fusion* (FusionMamba-style Xie et al. [2024], Li et al. [2024c]) adds a pre-scan confidence-gated blend that concatenates radar features into the image stream before the Mamba block, while the default (*Joint Modulation, main*) disables it. All rows are trained on the cleaned 160-sweep \mathbf{D}_{acc} with $\lambda_{\text{grad}} = 0.5$, matching Table 1. Best per column in **bold**.

Method	0–50 m		0–70 m		0–80 m	
	MAE (mm) ↓	RMSE (mm) ↓	MAE (mm) ↓	RMSE (mm) ↓	MAE (mm) ↓	RMSE (mm) ↓
Uniform FiLM	1094	3075	1437	4166	1564	4668
Horizon Modulation	964	2755	1251	3614	1352	3953
Readout Modulation	956	2792	1227	3672	1317	4012
RMS + pre-scan fusion	940	2749	1211	3657	1304	4019
Joint Modulation (main)	943	2784	1201	3611	1286	3920

Readout-only) and the lowest RMSE@80 (3920 vs. 3953 and 4012). On RMSE@50 the Horizon-only variant edges out the joint configuration by $\approx 1\%$, which we attribute to minor optimisation variance.

Pre-scan fusion adds nothing on top of RMS. The *RMS + pre-scan fusion* row adds a FusionMamba-style Xie et al. [2024], Li et al. [2024c] blend on top of Joint Modulation, reaching MAE@80 = 1304 — marginally worse than Joint Modulation alone (1286), with a small lead only at 0–50 m. Once radar modulates selection inside the scan, an additional pre-scan pathway adds no signal at the ranges that drive the headline metrics — complementing the Table 1 comparison against a full FusionMamba backbone.

5 Conclusion

We argued that radar should enter a Mamba-based depth backbone through the selection mechanism rather than the input stream, and realised this via Radar-Modulated Selection and the Multi-View Scan Pyramid. SemoDepth achieves state-of-the-art performance on nuScenes Caesar et al. [2020] across MAE and RMSE at every evaluation range, attains the lowest single-frame latency, and the ablation shows out-of-scan blending adds no accuracy on top of RMS — quantitative evidence that in-scan selection can match or replace out-of-scan fusion. The broader takeaway is conceptual: in sequence models with input-dependent recurrence, the selection mechanism itself can serve as a cross-modal interaction substrate, and we expect the recipe to extend to other sparse-plus-dense modality pairs (e.g., LiDAR–camera, radar–thermal) and to vision tasks beyond depth. One limitation remains: under the most camera-adversarial conditions (the 10% nighttime nuScenes Caesar et al. [2020] split), attention-based fusion remains competitive with selection-based fusion at short range. Overall, our findings suggest that cross-modal learning in sequence models should be reconsidered from the perspective of selection rather than representation — opening a new direction for multimodal sequence modelling beyond vision.

References

- Daniel Adolfsson, Martin Magnusson, Anas Alhashimi, Achim J Lilienthal, and Henrik Andreasson. Lidar-level localization with radar? the cfar approach to accurate, fast, and robust large-scale radar odometry in diverse environments. *IEEE Transactions on robotics*, 39(2):1476–1495, 2022.
- Igal Bilik, Oren Longman, Shahar Villeval, and Joseph Tabrikian. The rise of radar for autonomous vehicles: Signal processing solutions and future research directions. *IEEE signal processing Magazine*, 36(5):20–31, 2019.
- Holger Caesar, Varun Bankiti, Alex H Lang, Sourabh Vora, Venice Erin Liong, Qiang Xu, Anush Krishnan, Yu Pan, Giancarlo Baldan, and Oscar Beijbom. nuscenes: A multimodal dataset for autonomous driving. In *Proceedings of the IEEE/CVF conference on computer vision and pattern recognition*, pages 11621–11631, 2020.
- Xiaomeng Chu, Jiajun Deng, Guoliang You, Yifan Duan, Houqiang Li, and Yanyong Zhang. Rac-former: Towards high-quality 3d object detection via query-based radar-camera fusion. In *Proceedings of the IEEE/CVF Conference on Computer Vision and Pattern Recognition*, pages 17081–17091, 2025.
- Tri Dao and Albert Gu. Transformers are ssms: Generalized models and efficient algorithms through structured state space duality. *arXiv preprint arXiv:2405.21060*, 2024.
- Stefano Gasperini, Patrick Koch, Vinzenz Dallabetta, Nassir Navab, Benjamin Busam, and Federico Tombari. R4dyn: Exploring radar for self-supervised monocular depth estimation of dynamic scenes. In *2021 International Conference on 3D Vision (3DV)*, pages 751–760. IEEE, 2021.
- Andreas Geiger, Philip Lenz, Christoph Stiller, and Raquel Urtasun. Vision meets robotics: The kitti dataset. *The international journal of robotics research*, 32(11):1231–1237, 2013.
- Ionuț Grigore and Călin-Adrian Popa. Mambadepth: Enhancing long-range dependency for self-supervised fine-structured monocular depth estimation. *arXiv preprint arXiv:2406.04532*, 2024.
- Albert Gu and Tri Dao. Mamba: Linear-time sequence modeling with selective state spaces. *arXiv preprint arXiv:2312.00752*, 2023.
- Albert Gu, Karan Goel, and Christopher Ré. Efficiently modeling long sequences with structured state spaces. *arXiv preprint arXiv:2111.00396*, 2021.
- Zeyu Han, Jiahao Wang, Zikun Xu, Shuocheng Yang, Lei He, Shaobing Xu, Jianqiang Wang, and Keqiang Li. 4d millimeter-wave radar in autonomous driving: A survey. *arXiv preprint arXiv:2306.04242*, 2023.
- Han Li, Yukai Ma, Yaqing Gu, Kewei Hu, Yong Liu, and Xingxing Zuo. Radarcam-depth: Radar-camera fusion for depth estimation with learned metric scale. In *2024 IEEE International Conference on Robotics and Automation (ICRA)*, pages 10665–10672. IEEE, 2024a.
- Huadong Li, Minhao Jing, Wang Jin, Shichao Dong, Jiajun Liang, Haoqiang Fan, and Renhe Ji. Sparse beats dense: Rethinking supervision in radar-camera depth completion. In *European Conference on Computer Vision*, pages 127–143. Springer, 2024b.
- Zhe Li, Haiwei Pan, Kejia Zhang, Yuhua Wang, and Fengming Yu. Mambadfuse: A mamba-based dual-phase model for multi-modality image fusion. *arXiv preprint arXiv:2404.08406*, 2024c.
- Juan-Ting Lin, Dengxin Dai, and Luc Van Gool. Depth estimation from monocular images and sparse radar data. In *2020 IEEE/RSJ International Conference on Intelligent Robots and Systems (IROS)*, pages 10233–10240. IEEE, 2020.
- Zhiwei Lin, Zhe Liu, Zhongyu Xia, Xinhao Wang, Yongtao Wang, Shengxiang Qi, Yang Dong, Nan Dong, Le Zhang, and Ce Zhu. Rcbvdet: Radar-camera fusion in bird’s eye view for 3d object detection. In *Proceedings of the IEEE/CVF Conference on Computer Vision and Pattern Recognition*, pages 14928–14937, 2024.

- Yue Liu, Yunjie Tian, Yuzhong Zhao, Hongtian Yu, Lingxi Xie, Yaowei Wang, Qixiang Ye, Jianbin Jiao, and Yunfan Liu. Vmamba: Visual state space model. *Advances in neural information processing systems*, 37:103031–103063, 2024.
- Chen-Chou Lo and Patrick Vandewalle. Depth estimation from monocular images and sparse radar using deep ordinal regression network. In *2021 IEEE International Conference on Image Processing (ICIP)*, pages 3343–3347. IEEE, 2021.
- Yunfei Long, Daniel Morris, Xiaoming Liu, Marcos Castro, Punarjay Chakravarty, and Praveen Narayanan. Radar-camera pixel depth association for depth completion. In *Proceedings of the IEEE/CVF Conference on Computer Vision and Pattern Recognition*, pages 12507–12516, 2021.
- Andras Palffy, Ewoud Pool, Srimannarayana Baratam, Julian FP Kooij, and Dariu M Gavrilă. Multi-class road user detection with 3+ 1d radar in the view-of-delft dataset. *IEEE Robotics and Automation Letters*, 7(2):4961–4968, 2022.
- Akash Deep Singh, Yunhao Ba, Ankur Sarker, Howard Zhang, Achuta Kadambi, Stefano Soatto, Mani Srivastava, and Alex Wong. Depth estimation from camera image and mmwave radar point cloud. In *Proceedings of the IEEE/CVF Conference on Computer Vision and Pattern Recognition*, pages 9275–9285, 2023.
- Huawei Sun, Hao Feng, Julius Ott, Lorenzo Servadei, and Robert Wille. Cafnet: A confidence-driven framework for radar camera depth estimation. In *2024 IEEE/RSJ International Conference on Intelligent Robots and Systems (IROS)*, pages 2734–2740. IEEE, 2024.
- Jonas Uhrig, Nick Schneider, Lukas Schneider, Uwe Franke, Thomas Brox, and Andreas Geiger. Sparsity invariant cnns. In *2017 international conference on 3D Vision (3DV)*, pages 11–20. IEEE, 2017.
- Runzhong Wang, Junchi Yan, and Xiaokang Yang. Learning combinatorial embedding networks for deep graph matching. In *Proceedings of the IEEE/CVF international conference on computer vision*, pages 3056–3065, 2019.
- Yiran Wang, Jiaqi Li, Chaoyi Hong, Ruibo Li, Liusheng Sun, Xiao Song, Zhe Wang, Zhiguo Cao, and Guosheng Lin. Tacodepth: Towards efficient radar-camera depth estimation with one-stage fusion. In *Proceedings of the IEEE/CVF Conference on Computer Vision and Pattern Recognition*, pages 10523–10533, 2025.
- Xinyu Xie, Yawen Cui, Tao Tan, Xubin Zheng, and Zitong Yu. Fusionmamba: Dynamic feature enhancement for multimodal image fusion with mamba. *Visual Intelligence*, 2(1):37, 2024.
- Lihe Yang, Bingyi Kang, Zilong Huang, Xiaogang Xu, Jiashi Feng, and Hengshuang Zhao. Depth anything: Unleashing the power of large-scale unlabeled data. In *Proceedings of the IEEE/CVF conference on computer vision and pattern recognition*, pages 10371–10381, 2024.
- Lianghui Zhu, Bencheng Liao, Qian Zhang, Xinlong Wang, Wenyu Liu, and Xinggang Wang. Vision mamba: Efficient visual representation learning with bidirectional state space model. *arXiv preprint arXiv:2401.09417*, 2024.

A Technical appendices and supplementary material

A.1 Day/night breakdown on nuScenes val

Table 5 reports the day/night split on the nuScenes Caesar et al. [2020] val set, following the day/night protocol of TacoDepth Wang et al. [2025]: a scene is classified *night* when its description field contains “night” (case-insensitive), otherwise *day*, partitioning the val set into 5,282 daytime and 587 nighttime keyframes. Singh et al. and TacoDepth numbers are reproduced from TacoDepth; SemoDepth is evaluated under the identical protocol against single-sweep sparse LiDAR with predictions clamped to [0.5, 80] m, matching Table 1.

Table 5: Day/night quantitative breakdown on the nuScenes dataset Caesar et al. [2020]. Following TacoDepth Wang et al. [2025], scenes whose description field contains “night” form the nighttime split; the validation set partitions into 5,282 daytime and 587 nighttime keyframes. Best per column in **bold**.

Scene	Method	0–50 m		0–70 m		0–80 m	
		MAE (mm) ↓	RMSE (mm) ↓	MAE (mm) ↓	RMSE (mm) ↓	MAE (mm) ↓	RMSE (mm) ↓
Daytime	Singh et al. Singh et al. [2023] (CVPR’23)	1618.9	3613.0	1924.7	4359.2	2017.9	4632.5
	TacoDepth Wang et al. [2025] (CVPR’25)	1389.5	3227.3	1680.9	3897.1	1782.4	4092.3
	SemoDepth (Ours)	857.9	2606.3	1105.2	3416.5	1190.2	3731.1
Nighttime	Singh et al. Singh et al. [2023] (CVPR’23)	2340.8	4683.8	2863.9	5935.4	3012.9	6338.3
	TacoDepth Wang et al. [2025] (CVPR’25)	1673.6	3631.4	1944.8	4425.3	2207.6	4574.8
	SemoDepth (Ours)	1709.4	4381.5	2061.9	5358.2	2146.1	5621.7
Overall	Singh et al. Singh et al. [2023] (CVPR’23)	1727.7	3746.8	2073.2	4590.7	2179.3	4898.7
	TacoDepth Wang et al. [2025] (CVPR’25)	1423.6	3275.8	1712.6	3960.5	1833.4	4150.2
	SemoDepth (Ours)	943.0	2783.9	1200.9	3610.7	1285.8	3920.2

Daytime (90% of frames). SemoDepth wins every column, with MAE margins of 33–38% over TacoDepth and 41–47% over Singh et al.; the 0–80 m gain over TacoDepth is –33% MAE (1190 vs. 1782) and –9% RMSE (3731 vs. 4092). Daytime is the regime in which radar’s metric anchor and the in-scan selection have the most leverage, and this split dominates the aggregate metrics in Table 1 due to its larger proportion of frames.

Nighttime (10% of frames). SemoDepth retains the lead over Singh et al. across all six columns. Against TacoDepth, SemoDepth attains the best MAE@80 (2146 vs. 2208, –2.8%) but trails on the shorter-range metrics. Night is the regime in which the camera signal is weakest, so tail-outlier pixels — which dominate RMSE@80 and contribute most of the residual MAE error — are more prevalent than in daytime; in this regime a strong attention-based fusion competes more closely with a selection-based one. We disclose this rather than aggregate it away: the in-scan-selection design wins decisively where image evidence is informative (typical pixels, daytime conditions) and remains competitive at the longest range under the most camera-adversarial conditions, but does not always lead at short range when monocular cues fail outright.

A.2 Inverse-depth metrics on ZJU-4DRadarCam

Table 6 reports inverse-depth metrics (iMAE, iRMSE) for the ZJU-4DRadarCam comparison whose linear-metre MAE and RMSE appear in Table 2. SemoDepth attains the best iMAE and iRMSE at every evaluation range, with ~18% iMAE and ~8% iRMSE drops over TacoDepth — consistent with the typical-pixel-gain pattern observed on nuScenes (§4.3).

Table 6: Inverse-depth metrics (iMAE, iRMSE) on the ZJU-4DRadarCam dataset Li et al. [2024a], complementing the linear-metre MAE/RMSE in Table 2. Baseline numbers are as reported by TacoDepth Wang et al. [2025]. Best per column in **bold**.

Method	0–50 m		0–70 m		0–80 m	
	iMAE (km ⁻¹) ↓	iRMSE (km ⁻¹) ↓	iMAE (km ⁻¹) ↓	iRMSE (km ⁻¹) ↓	iMAE (km ⁻¹) ↓	iRMSE (km ⁻¹) ↓
DORN Lo and Vandewalle [2021]	19.8	31.9	19.8	31.9	19.9	31.9
Singh et al. Singh et al. [2023]	18.1	35.3	18.0	35.2	17.9	35.1
TacoDepth Wang et al. [2025]	12.8	25.0	12.7	24.9	12.7	24.9
SemoDepth (Ours)	10.4	22.8	10.4	22.8	10.4	22.8

A.3 Qualitative results on ZJU-4DRadarCam

Figure 3 shows SemoDepth predictions on four randomly drawn frames from the ZJU-4DRadarCam Li et al. [2024a] test split, alongside the input radar returns and single-sweep LiDAR ground truth. Public weights or runnable inference pipelines for the ZJU baselines (DORN Lo and Vandewalle [2021], Singh et al. Singh et al. [2023], TacoDepth Wang et al. [2025]) were not available at submission time, so we showcase SemoDepth’s prediction quality directly against ground truth rather than against re-trained baselines. Per-frame MAE / RMSE in millimetres are computed against single-sweep sparse LiDAR over 0–80 m, matching the protocol of Table 2.

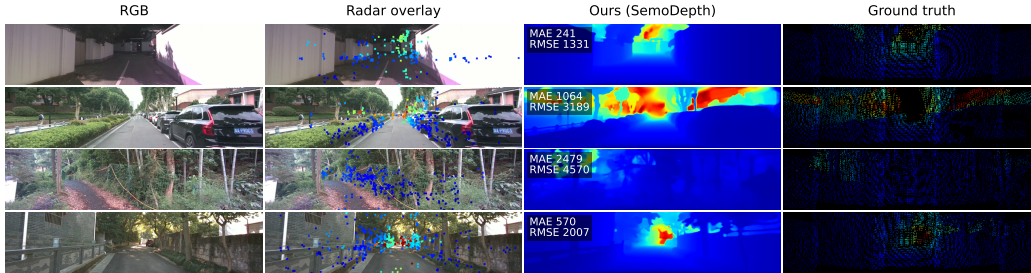


Figure 3: Qualitative results on the ZJU-4DRadarCam dataset Li et al. [2024a]. Columns: RGB; sparse radar returns overlaid on the RGB; SemoDepth prediction; single-sweep LiDAR ground truth. Per-frame MAE / RMSE in millimetres against single-sweep sparse LiDAR over 0–80 m; jet colormap clipped at 80 m. Frames are randomly drawn from the test split (seed 0, indices 1105, 2093, 2607, 3481 of the 4,097 test frames) so the spread of MAE values reflects test-set variability rather than cherry-picking. The fine-grained vehicle and lane geometry recovered by SemoDepth despite the radar input averaging only ~ 380 returns per frame illustrates how in-scan radar selection propagates each return’s metric anchor through the full sequence.

A.4 Complete ablation results

Table 7 reports the full ablation summarised in Table 4, including iMAE and iRMSE at the 0–80 m range. The MVSP-load-bearing argument is reinforced on the inverse-depth metric: Joint Modulation reduces iMAE@80 from 5.14 to 4.22 (−18%) over Uniform-FiLM, matching the MAE@80 improvement. Joint Modulation also attains the lowest iMAE@80 (4.22 vs. 4.41 Horizon-only, 4.36 Readout-only); on iRMSE@80 the Horizon-only variant edges out the joint configuration by $\approx 1\%$, attributable to minor optimisation variance. The *RMS + pre-scan fusion* configuration’s iRMSE@80 (11.03) is also marginally worse than Joint Modulation alone (10.85), consistent with the MAE@80 pattern.

Table 7: Complete ablation table on the nuScenes dataset Caesar et al. [2020], including inverse-depth analogues iMAE and iRMSE at the 0–80 m range. Long-form companion to Table 4; supervision and bolding conventions match. Best per column in **bold**.

Method	0–50 m		0–70 m		0–80 m		iMAE (km ^{−1}) ↓	iRMSE (km ^{−1}) ↓
	MAE (mm) ↓	RMSE (mm) ↓	MAE (mm) ↓	RMSE (mm) ↓	MAE (mm) ↓	RMSE (mm) ↓		
Uniform FiLM	1094	3075	1437	4166	1564	4668	5.14	13.44
Horizon Modulation	964	2755	1251	3614	1352	3953	4.41	10.74
Readout Modulation	956	2792	1227	3672	1317	4012	4.36	10.89
RMS + pre-scan fusion	940	2749	1211	3657	1304	4019	4.29	11.03
Joint Modulation (main)	943	2784	1201	3611	1286	3920	4.22	10.85

A.5 Effect of horizon cleaning across RMS variants

The headline SemoDepth row in Table 1 is trained on the filtered 160-sweep accumulated supervision (§4.2) with $\lambda_{\text{grad}} = 0.5$. Here we ablate that supervision choice across the three RMS variants of §3.2, holding architecture and every other hyperparameter fixed within each pair: the only differences between rows of the same method are (i) which \mathbf{D}_{acc} manifest is used, and (ii) λ_{grad} , which is admissible at 0.5 only after the filtering step removes the dominant accumulation artefacts that gradient matching would otherwise reinforce. We report the best-MAE@80 checkpoint per run.

The pattern is consistent across architectures. Filtering unambiguously improves every RMSE-class metric for every variant: between −10.0% and −10.3% on RMSE@80, and between −10.6% and −26.8% on iRMSE@80. The largest iRMSE@80 wins are on the single-pathway variants (Readout: −26.8%, Horizon: −20.0%), exactly the configurations whose raw-supervised iRMSE@80 was most inflated by tail-pixel residuals (Table 4, raw values 14.87 and 13.43). On linear-metre MAE the cleaning effect is more variable: an improvement on Joint Modulation (−2.0% at 0–80 m), neutral on Readout Modulation (−0.1%), and a slight regression on Horizon Modulation (+2.6%). This

Table 8: Effect of horizon cleaning across the three RMS variants on the nuScenes dataset Caesar et al. [2020]. Each method appears twice: *raw* 160-sweep \mathbf{D}_{acc} with $\lambda_{\text{grad}} = 0$ (the standard CaFNet/SBD accumulation), and *cleaned* 160-sweep \mathbf{D}_{acc} produced by the AND-gated drop pipeline of §4.2 with $\lambda_{\text{grad}} = 0.5$. Bold marks the better supervision regime within each architecture pair. The Joint Modulation cleaned row is also the headline SemoDepth (Ours) configuration in Table 1.

Method	Supervision	0–50 m		0–70 m		0–80 m			
		MAE (mm) ↓	RMSE (mm) ↓	MAE (mm) ↓	RMSE (mm) ↓	MAE (mm) ↓	RMSE (mm) ↓	iMAE (km ⁻¹) ↓	iRMSE (km ⁻¹) ↓
Horizon Modulation	Raw, $\lambda_{\text{grad}} = 0$	911	2895	1204	3908	1318	4393	4.38	13.43
	Cleaned, $\lambda_{\text{grad}} = 0.5$	964	2755	1251	3614	1352	3953	4.41	10.74
Readout Modulation	Raw, $\lambda_{\text{grad}} = 0$	913	2914	1203	3970	1318	4471	4.54	14.87
	Cleaned, $\lambda_{\text{grad}} = 0.5$	956	2792	1227	3672	1317	4012	4.36	10.89
Joint Modulation (main)	Raw, $\lambda_{\text{grad}} = 0$	900.7	2849.5	1204.5	3900.3	1311.9	4362.9	4.17	12.14
	Cleaned, $\lambda_{\text{grad}} = 0.5$	943.0	2783.9	1200.9	3610.7	1285.8	3920.2	4.22	10.85

follows from the distribution of residuals: removed pixels are few but carry large errors under raw supervision; squared-error metrics penalise these tail pixels disproportionately and therefore record the largest improvements. MAE, dominated by the much larger mass of correctly-supervised pixels, moves much less and is within run-to-run optimisation noise.

A.6 Limitations

We discuss four limitations of the present work, in decreasing order of consequence for the claims of §4.

Modality scope. SemoDepth is evaluated on front-camera + automotive radar only. The architectural argument for in-scan selection (§3.2) is modality-agnostic, but we do not empirically validate the recipe on other sparse-plus-dense modality pairs (LiDAR + camera, radar + thermal, depth + event); the conceptual transfer claim in §3 is therefore not empirically validated in this work.

Statistical variability. The main configuration in Table 1 is reported as the mean and standard deviation over three independently seeded training runs. Ablation rows (Tables 4, 8) and the day/night breakdown (§A.1) are reported from single seeded runs, since multi-seed ablations are uncommon in radar-camera depth completion Li et al. [2024a], Wang et al. [2025], Sun et al. [2024], Li et al. [2024b]. Tail-sensitive metrics — iRMSE at the longest range, the nighttime subsplit — have run-to-run variability of similar order to some of the smaller cross-method gaps and should be interpreted as such.

Sensitivity to radar sparsity. The architectural margin shrinks on ZJU-4DRadarCam Li et al. [2024a] (5–8% MAE drop over TacoDepth) compared with nuScenes Caesar et al. [2020] (~30% MAE drop). The shift follows from concrete radar quality differences: nuScenes radar is 3D (azimuth + range, no elevation) and produces 40–100 returns per front-camera frame, whereas ZJU’s 4D radar adds elevation and yields ~380 returns per frame — roughly an order of magnitude denser. Each ZJU return constrains a 3D point rather than a height-ambiguous 2D plane, leaving baselines that fuse radar at the feature level less work to do, and leaving in-scan selection less headroom to add via per-token propagation. ZJU’s single-campus collection also reduces the environmental variability that selection-based fusion exploits per-token. We therefore expect the gap to widen on a 3D-radar dataset of comparable scale to nuScenes, but have not yet validated this empirically.

Supervision artefacts. The upper-image filtering step (§4.2) reduces but does not fully eliminate accumulation noise in \mathbf{D}_{acc} , leaving small far-field artefacts that do not affect the metrics but are visible in the qualitative depth maps. We leave a more principled treatment of dynamic-object accumulation to future work.

We do not observe additional architectural failure modes beyond these in our experiments. SemoDepth degrades gracefully when radar is sparse (the state update remains image-only by construction; §3.2), so radar dropout reduces accuracy smoothly toward the image-only baseline rather than producing failure modes. Radar *noise* (as opposed to sparsity) is a separate, untested concern: because RMS modulates Δ_t and \mathbf{C}_t inside the recurrence, systematically incorrect radar anchors could in principle propagate through the scan rather than being filtered at a feature blend. The zero-initialised construction provides partial protection — gates that find radar uninformative learn small weights — but we have not stress-tested noise injection, so this remains a hypothesised rather than observed failure mode.

A.7 Broader impacts

Positive. Robust, low-cost, all-weather metric depth perception is a near-term enabler for safer driver-assistance systems on vehicles that cannot accommodate the cost or power budget of automotive LiDAR. By inheriting radar’s all-weather operating envelope and contributing a fusion mechanism (RMS) that is graceful under sparse radar returns, SemoDepth lowers the perception-stack cost floor for assisted-driving features (forward-collision warning, automatic emergency braking, adaptive cruise control) that disproportionately benefit users in cost-sensitive markets and adverse weather environments where camera-only stacks degrade.

Negative. Improved radar-camera scene understanding is dual-use: the same depth predictions that aid driver-assistance can be incorporated into surveillance pipelines, military radar-camera systems, or other non-civilian deployments. Beyond explicit dual-use, depth completion deployed at scale shares the standard concerns of automated perception — failures concentrated on rare scene types or atypical objects (e.g., pedestrians with unusual silhouettes or in non-Western dress codes) can have safety-critical consequences if downstream planners assume perception accuracy is uniform across scenes. We do not study geographic or demographic robustness in this paper; both the nuScenes Caesar et al. [2020] and ZJU-4DRadarCam Li et al. [2024a] datasets are collected in narrow geographic regions (Boston/Singapore and a single ZJU campus respectively), which limits how confidently any quantitative claim transfers to under-represented driving environments.

Mitigations. The released checkpoints are research artefacts, not production-grade ADAS components, and we recommend they be used only for further research; downstream deployment should be paired with the appropriate scene-conditional evaluation and out-of-distribution monitoring. Beyond this, the techniques described do not introduce fundamentally new harmful capabilities beyond existing radar-camera depth methods Sun et al. [2024], Wang et al. [2025], Li et al. [2024b]; we therefore do not impose access controls or staged release.

A.8 Compute resources

Hardware. All experiments are run on a single workstation with one NVIDIA RTX PRO 6000 Blackwell Workstation Edition GPU (96 GB VRAM, CUDA 13.0). bf16 mixed-precision training is used throughout (§4.2); peak training-time VRAM is approximately 24 GB at batch size 12, well below the device limit, but the Mamba selective-scan kernel benefits noticeably from Blackwell-class throughput on the $L \times D$ token sequences encountered at the coarsest MVSP tier.

Per-run cost. A single nuScenes Caesar et al. [2020] training run ($n_{\text{train}} = 27,430$, batch 12, 50 epochs) takes approximately 26 hours wall-clock; one ZJU-4DRadarCam Li et al. [2024a] run ($n_{\text{train}} = 26,055$, batch 12, 100 epochs) takes approximately 24 hours. The horizon-cleaning preprocessing (§4.2) is a one-time pass over the train+val split and takes approximately 40 minutes on 40 CPU threads with the nuScenes devkit; once cached, it adds no per-epoch cost. Inference, as reported in §4.4, runs at 26.8 ms per frame at the nuScenes input resolution of 900×1600 .

Project compute. The full set of reported configurations (Table 1, the three RMS variants of Table 4, the cleaning ablation of Table 8, and the day/night evaluation of Table 5) accounts for approximately 13 GPU-days. Including preliminary runs, failed configurations, and ablations that did not make it into the paper (early KNN-graph radar branches, alternative scan directions, alternative supervision schedules), total project compute is approximately 25 GPU-days on the same single-GPU workstation.

A.9 Code and reproducibility

The released code repository accompanies this submission as an anonymised tarball in the supplemental material and is structured to reproduce every quantitative result in Tables 1, 4, 8, and 5 end-to-end from the published nuScenes Caesar et al. [2020] and ZJU-4DRadarCam Li et al. [2024a] releases.

Repository contents. The top-level layout separates model code (`mambadepth_fusion/`, with `model/`, `data/`, `train/`, `utils/` subpackages), entry-point scripts (`scripts/`, including `train_nuscenes.py`, `train_zju.py`, `eval_nuscenes.py`, the LiDAR accumulation utility, and the horizon-cleaning preprocessing pipeline of §4.2), and unit tests (`tests/`) that include the zero-initialisation parity check that numerically verifies Eq. (5) on a CUDA device.

Documentation. The README provides environment setup (Python, CUDA, version-pinned `mamba-ssm` and `causal-conv1d`; see also Table 9), the exact commands used to reproduce each headline configuration, and a brief description of every CLI flag exposed by the training scripts. Per-script behaviour is additionally documented in the file-header docstrings.

Reproduction recipe. Following the dataset preparation steps in the README (download, devkit installation, then a one-time invocation of the LiDAR-accumulation and horizon-cleaning scripts), each row of Table 1 is reproduced by a single `python scripts/train_nuscenes.py` or `python scripts/train_zju.py` command with the configuration flags listed in the README. All experiments are run with fixed random seeds; seeds are specified in the provided training scripts. Best-checkpoint selection is performed automatically against the validation split during training.

A.10 Licenses for existing assets

Table 9 lists every external dataset, code package, and pretrained weight used in this work, the version we relied on, the license under which it is distributed, and the role it plays in our pipeline. All assets are used in compliance with their respective licenses; nuScenes Caesar et al. [2020] is used under its non-commercial research license, and no asset is redistributed in a form that would constitute a derivative work requiring relicensing.

Table 9: External assets used in SemoDepth. Versions correspond to the snapshot used for the experiments reported in this paper. Licenses are summarised; the full license texts ship with each asset’s release. URLs are intentionally omitted from this anonymised submission and will be added on de-anonymisation.

Asset	Version	License	Role in this work
nuScenes Caesar et al. [2020]	v1.0-trainval	CC BY-NC-SA 4.0	Primary benchmark; train/val/test
ZJU-4DRadarCam Li et al. [2024a]	official release	per upstream repo	Secondary benchmark; train/test
nuscenes-devkit	1.1.x	Apache 2.0	LiDAR accumulation, projection
ResNet-34 (torchvision)	ImageNet1K-V1	BSD-3-Clause	Image encoder initialisation
<code>mamba-ssm</code>	1.2.x	Apache 2.0	Selective-scan CUDA kernel
<code>causal-conv1d</code>	1.2.x	BSD-3-Clause	Mamba dependency
PyTorch	2.x	BSD-3-Clause	Training framework
PCA-GM Wang et al. [2019]	reference impl.	per upstream repo	Radar GSE building block
TacoDepth Wang et al. [2025]	paper formulae	— (no code reused)	Comparison baseline; loss reference
RadarCam-Depth Li et al. [2024a]	ZJU release	per upstream repo	Comparison baseline; ZJU dataset host

We additionally cite each prior method we reproduce or compare against in Table 1 (Singh et al. Singh et al. [2023], CaFNet Sun et al. [2024], Li et al. Li et al. [2024b]) at the point of use. No assets are redistributed in this submission; the released code consists of newly-written training, evaluation, and visualisation scripts that depend on the listed assets through their public package interfaces.